

# Synchronization of Parallel Single-Phase Inverters With Virtual Oscillator Control

Brian B. Johnson<sup>†</sup>, *Member, IEEE*, Sairaj V. Dhople, *Member, IEEE*,  
Abdullah O. Hamadeh, and Philip T. Krein, *Fellow, IEEE*

**Abstract**—A method to synchronize and control a system of parallel single-phase inverters without communication is presented. Inspired by the phenomenon of synchronization in networks of coupled oscillators, we propose that each inverter be controlled to emulate the dynamics of a nonlinear dead-zone oscillator. As a consequence of the electrical coupling between inverters, they synchronize and share the load in proportion to their ratings. We outline a sufficient condition for global asymptotic synchronization and formulate a methodology for controller design such that the inverter terminal voltages oscillate at the desired frequency, and the load voltage is maintained within prescribed bounds. We also introduce a technique to facilitate the seamless addition of inverters controlled with the proposed approach into an energized system. Experimental results for a system of three inverters demonstrate power sharing in proportion to power ratings for both linear and nonlinear loads.

**Index Terms**—Distributed ac power systems, inverters, microgrids, nonlinear control, oscillators, synchronization, uninterruptible power supplies, voltage source inverters.

## I. INTRODUCTION

SYSTEMS of parallel inverters are integral elements of distributed ac power systems in applications such as uninterruptible power supplies, microgrids, and renewable energy systems [1]–[8]. Critical design and control objectives in such systems include: i) minimizing communication between inverters, ii) maintaining system stability and synchronization in spite of load variations, iii) regulating the system voltage and frequency, and iv) ensuring the inverters share the load in proportion to their ratings. Focused on these challenges, this paper presents a method to synchronize and control a system of parallel single-phase inverters without communication. Inspired by the phenomenon of synchronization in networks of coupled oscillators, we propose that each inverter be controlled to emulate the dynamics of a nonlinear dead-zone oscillator.

<sup>†</sup> Corresponding author.

B. B. Johnson is with the Power Systems Engineering Center at the National Renewable Energy Laboratory, Golden, CO, 80401 (e-mail: brian.johnson@NREL.GOV, tel: 303-275-3967), but has written this article outside the scope of his employment; S. V. Dhople is with the Department of Electrical and Computer Engineering at the University of Minnesota, Minneapolis, MN (email: sdhople@UMN.EDU); A. O. Hamadeh is with the Department of Mechanical Engineering at the Massachusetts Institute of Technology, Cambridge, MA (e-mail: ahamadeh@MIT.EDU); P. T. Krein is with the Department of Electrical and Computer Engineering at the University of Illinois, Urbana, IL (email: krein@ILLINOIS.EDU).

B. B. Johnson was supported in part by a National Science Foundation Graduate Research Fellowship and the Grainger Center for Electric Machinery and Electromechanics at the University of Illinois.

P. T. Krein was supported in part by the Global Climate and Energy Project at Stanford University.

Leveraging the intrinsic electrical coupling between inverters, global asymptotic synchronization can be guaranteed with no additional communication. Additionally, the synchronization condition is demonstrated to be independent of the number of inverters in the system and the load characteristics. The proposed control paradigm is therefore robust (independent of load), resilient (requires no communication), and modular (independent of the number of inverters). In the remainder of the manuscript, we refer to the proposed method as *virtual oscillator control* (VOC) to emphasize the fact that each inverter is digitally controlled to emulate the dynamics of a nonlinear oscillator.

The analytical framework that underlies the proposed control method was outlined in [12], [13], where sufficient conditions were derived for synchronization in a system of identical nonlinear oscillators connected to a common node through identical branch impedances. Subsequently in [14], we demonstrated applications of the oscillator-based controller in three-phase, low-inertia microgrids with a high penetration of photovoltaic generation. In [12], [14], it was assumed that all inverters had identical power ratings and that the load was a passive impedance. Building on our previous efforts, the main contributions of this paper are the following: i) a synchronization condition is developed which applies to both linear and nonlinear loads, ii) the controller and output-filter design approaches are demonstrated to result in the inverters sharing the load power in proportion to their power ratings, iii) a parameter selection methodology is presented such that the inverter terminal voltages oscillate at the desired frequency and the load voltage is maintained between prescribed upper and lower bounds, iv) a technique for adding inverters into an energized system with minimal transients is introduced, and v) experimental results demonstrate seamless inverter addition and power sharing for linear and nonlinear loads.

Control strategies that do not necessitate communication in systems of parallel inverters have predominantly been inspired by the idea of droop control [15]–[22]. The premise of this method is to modulate the voltage and frequency of islanded inverters such that they mimic the behavior of synchronous generators in bulk power systems [15]. In particular, the inverter voltage and frequency are controlled to be inversely proportional to the real and reactive power output, respectively [23]–[25]. To overcome shortcomings associated with load-sharing accuracy and system frequency/voltage deviations, recent efforts have focused on the overlay of a communication network between inverters to implement secondary- and tertiary-level controls [17], [26]–[28]. In contrast, the experi-

mental results in this work demonstrate that with the proposed approach, the system frequency exhibits minimal deviations with variations in load, and the load voltage can be maintained between prescribed bounds without communication. The ease of controller implementation is an added advantage; in particular, compared to droop control and related variants, VOC does not require real and reactive power calculations, explicit frequency and voltage amplitude commands, or any trigonometric functions.

Synchronization phenomena in networks of coupled oscillators have received attention in a variety of disciplines including cardiology, neural processes, superconductor physics, communications, and chemistry [29]–[33]. Of particular relevance to the power engineering community, the Kuramoto oscillator model was recently applied to study synchronization in bulk power systems [34] and droop-controlled inverters [35], [36]. Inspirational to this work, the notion of passivity was used in [37] to analyze synchronization of inverters controlled as nonlinear oscillators. As described subsequently, the analytical approach and oscillator model adopted in this work here are fundamentally different from that in [37]; it is also worth mentioning that the controller proposed in this work does not require an additional PI regulator for voltage regulation as in [37]. In general, passivity-based approaches used to examine synchronization require the formulation of a storage function (global Lyapunov function) that is proportional to signal differences. Conditions for synchronization are then obtained by requiring the storage function to decay to zero along system trajectories [38]–[41]. Given that it is difficult to construct storage functions that monotonically decay to zero when the network contains energy storage elements (i.e., inductors and capacitors), passivity-based approaches are, in general, difficult to apply in these settings.

Leveraging the theoretical foundations in [42]–[44], we use the concept of  $\mathcal{L}_2$  input-output stability to prove synchronization. In general, the  $\mathcal{L}_2$  gain of a system provides a measure of the maximum possible amplification from input to output. Systems that have a finite  $\mathcal{L}_2$  gain are said to be *finite-gain  $\mathcal{L}_2$  stable* [45], [46]. To prove synchronization, we first construct a coordinate-transformed *differential system* based on signal differences. Then, by ensuring the differential system is finite-gain  $\mathcal{L}_2$  stable, we can prove that signal differences decay to zero, congruently demonstrating synchronization in the original coordinates.

The remainder of this manuscript is organized as follows: In Section II, we establish notation and present a few essential mathematical preliminaries. Detailed descriptions of the nonlinear dead-zone oscillator and the circuit equations that capture the network dynamics are presented in Section III. A coordinate transformation is then utilized in Section IV to analyze the corresponding system based on signal differences. Methods for controller design, implementation, and inverter addition are given in Section V, followed by experimental results in Section VI. Finally, concluding remarks and directions for future work are outlined in Section VII.

## II. PRELIMINARIES

Given the  $N$ -tuple  $\{u_1, \dots, u_N\}$ , denote the corresponding column vector as  $u = [u_1, \dots, u_N]^T$ , where  $(\cdot)^T$  denotes transposition. Denote the  $N \times N$  identity matrix as  $I$ , and the  $N$ -dimensional vectors of all ones and zeros as  $\mathbf{1}$  and  $\mathbf{0}$ , respectively.

The Laplace transform of the continuous-time function  $u(t)$  is denoted as  $u(s)$ , where  $s = \rho + j\omega \in \mathbb{C}$  and  $j = \sqrt{-1}$ .

The Euclidean norm of a complex vector,  $u$ , is denoted as  $\|u\|_2$  and is defined as

$$\|u\|_2 := \sqrt{u^* u}, \quad (1)$$

where  $(\cdot)^*$  signifies the conjugate transpose. The space of all piecewise continuous functions such that

$$\|u\|_{\mathcal{L}_2} := \sqrt{\int_0^\infty u(t)^T u(t) dt} < \infty, \quad (2)$$

is denoted as  $\mathcal{L}_2$ , where  $\|u\|_{\mathcal{L}_2}$  is referred to as the  $\mathcal{L}_2$  norm of  $u$  [46]. If  $u \in \mathcal{L}_2$ , then  $u$  is said to be *bounded*.

A causal system,  $H$ , with input  $u$  and output  $y$  is *finite-gain  $\mathcal{L}_2$  stable* if there exist finite, non-negative constants,  $\gamma$  and  $\eta$ , such that

$$\|y\|_{\mathcal{L}_2} =: \|H(u)\|_{\mathcal{L}_2} \leq \gamma \|u\|_{\mathcal{L}_2} + \eta, \quad \forall u \in \mathcal{L}_2. \quad (3)$$

The smallest value of  $\gamma$  for which there exists a  $\eta$  such that (3) is satisfied is called the  $\mathcal{L}_2$  gain of the system. The  $\mathcal{L}_2$  gain of  $H$ , denoted as  $\gamma(H)$ , provides a measure of the largest amplification imparted to the input signal,  $u$ , as it propagates through  $H$ . If  $H$  is linear and can be represented by the transfer matrix  $H(s) \in \mathbb{C}^{N \times N}$ , it can be shown that the  $\mathcal{L}_2$  gain of  $H$  is equal to its  $\mathcal{H}$ -infinity norm, denoted by  $\|H\|_\infty$ , and defined as

$$\gamma(H) = \|H\|_\infty := \sup_{\omega \in \mathbb{R}} \frac{\|H(j\omega)u(j\omega)\|_2}{\|u(j\omega)\|_2}, \quad (4)$$

where  $\|u(j\omega)\|_2 = 1$ , provided that all poles of  $H(s)$  have strictly negative real parts [45]. Note that if  $H(s)$  is a single-input single-output transfer function such that  $H(s) \in \mathbb{C}$ , then  $\gamma(H) = \|H\|_\infty = \sup_{\omega \in \mathbb{R}} \|H(j\omega)\|_2$ .

A construct we will find particularly useful in assessing signal differences is the  $N \times N$  *projector matrix* [39], [40], [43], which is denoted by  $\Pi$ , and defined as

$$\Pi := I - \frac{1}{N} \mathbf{1}\mathbf{1}^T. \quad (5)$$

For a vector  $u$ , we define  $\tilde{u} := \Pi u$  to be the corresponding *differential vector* [39], [40], [42]–[44]. It can be shown that [43], [44]

$$\tilde{u}(t)^T \tilde{u}(t) = (\Pi u(t))^T (\Pi u(t)) = \frac{1}{2N} \sum_{j=1}^N \sum_{k=1}^N (u_j(t) - u_k(t))^2, \quad (6)$$

which implies that  $u_j = u_k$  for  $j, k = 1, \dots, N$  if and only if  $\tilde{u} = 0$ .

A causal system with input  $u$  and output  $y$  is said to be *differentially finite  $\mathcal{L}_2$  gain stable* if there exist finite, non-negative constants,  $\tilde{\gamma}$  and  $\tilde{\eta}$ , such that

$$\|\tilde{y}\|_{\mathcal{L}_2} \leq \tilde{\gamma} \|\tilde{u}\|_{\mathcal{L}_2} + \tilde{\eta}, \quad \forall \tilde{u} \in \mathcal{L}_2, \quad (7)$$

where  $\tilde{y} = \Pi y$ . The smallest value of  $\tilde{\gamma}$  for which there exists a non-negative value of  $\tilde{\eta}$  such that (7) is satisfied is referred to as the *differential  $\mathcal{L}_2$  gain* of  $H$ . In general, the differential  $\mathcal{L}_2$  gain of a system provides a measure of the largest amplification imparted to input signal differences.

Finally, the RMS values of voltages and currents are denoted by  $V$  and  $I$ , respectively, and average power is denoted by  $P$ .

### III. SYSTEM DESCRIPTION

In this section, we first introduce the nonlinear dead-zone oscillator model that the inverters are controlled to emulate. Next, we outline the circuit equations that describe the system of parallel inverters controlled with the proposed approach.

#### A. The Nonlinear Dead-zone Oscillator

The electrical schematic of the nonlinear dead-zone oscillator is shown in Fig. 1(a). The construction of the proposed oscillator is inspired by the well-known Van der Pol oscillator [39], [40]. The linear subsystem of the oscillator is a passive  $RLC$  circuit with impedance

$$z_{\text{osc}}(s) = R \parallel sL \parallel (sC)^{-1} = \frac{\frac{1}{C}s}{s^2 + \frac{1}{RC}s + \frac{1}{LC}}. \quad (8)$$

The voltage dependent current source is a static nonlinear function,  $g(v) = -i_g(v)$ , parameterized by  $\sigma, \varphi \in \mathbb{R}^+$ , and defined as

$$g(v) = f(v) - \sigma v, \quad (9)$$

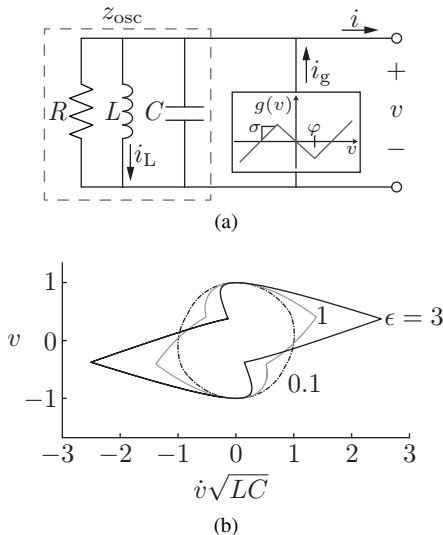


Figure 1: (a) Electrical schematic of the dead-zone oscillator. (b) Phase-plot of steady-state limit-cycles in the proposed nonlinear oscillator for different values of  $\epsilon = \sqrt{L/C}(\sigma - 1/R)$ .

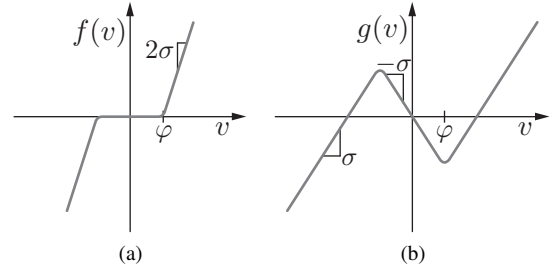


Figure 2: The dead-zone function  $f(v)$  in (a) and the nonlinear voltage-dependent current source  $g(v)$  in (b) are illustrated for the proposed dead-zone oscillator.

where  $f(v)$  is a dead-zone function with slope  $2\sigma$ :

$$f(v) = \begin{cases} 2\sigma(v - \varphi) & v > \varphi \\ 0 & |v| \leq \varphi \\ 2\sigma(v + \varphi) & v < -\varphi \end{cases}. \quad (10)$$

Note that with this definition, we have

$$\max_{v \in \mathbb{R}} \left| \frac{d}{dv} g(v) \right| = \sigma < \infty. \quad (11)$$

The functions  $f(\cdot)$  and  $g(\cdot)$  are illustrated in Figs. 2(a) and 2(b), respectively.

The oscillator dynamics are described by the following set of nonlinear differential equations:

$$\begin{cases} \frac{dv}{dt} = \frac{1}{C} \left( \sigma - \frac{1}{R} \right) v - f(v) - i_L - i \\ \frac{di_L}{dt} = \frac{v}{L} \end{cases}. \quad (12)$$

Applying Liénard's theorem, it can be shown that the proposed oscillator with the dynamics described by (12) has a unique and stable limit cycle if  $\sigma > 1/R$  [12], [45]. We plot the steady-state limit cycles of the proposed oscillator for different values of  $\epsilon := \sqrt{L/C}(\sigma - 1/R)$  in Fig. 1(b). It is evident that for small values of  $\epsilon$ , the phase plot resembles a unit circle, which implies that the voltage oscillation approximates an ideal sinusoid in the time-domain.

Intuitively, the oscillations result from a periodic energy exchange between the passive  $RLC$  circuit and the nonlinear current source at (approximately) the resonant frequency of the  $LC$  circuit,  $1/\sqrt{LC}$ . As can be inferred from Fig. 2(b), the nonlinear subsystem acts as a resistor (with resistance  $1/\sigma$ ) for  $vg(v) > 0$ , and as a power source for  $vg(v) < 0$ . This causes the amplitude of small oscillations to increase, while large oscillations are damped.

#### B. Fundamentals of System Design

Consider the system of parallel single-phase inverters in Fig. 3(a). The premise of VOC is to ensure that the inverters emulate the dynamics of dead-zone oscillators when the differential equations in (12) are programmed onto their digital controllers. The system of inverters with VOC in Fig. 3(a) can be modeled as shown in Fig. 3(b), where the controller details are depicted explicitly and the controllable voltage sources represent the averaged voltages across each set of H-bridge terminals. As illustrated in Fig. 3(b), the current sensed at the output of the  $j^{\text{th}}$  inverter is scaled by  $\kappa_j^{-1} i$  and extracted

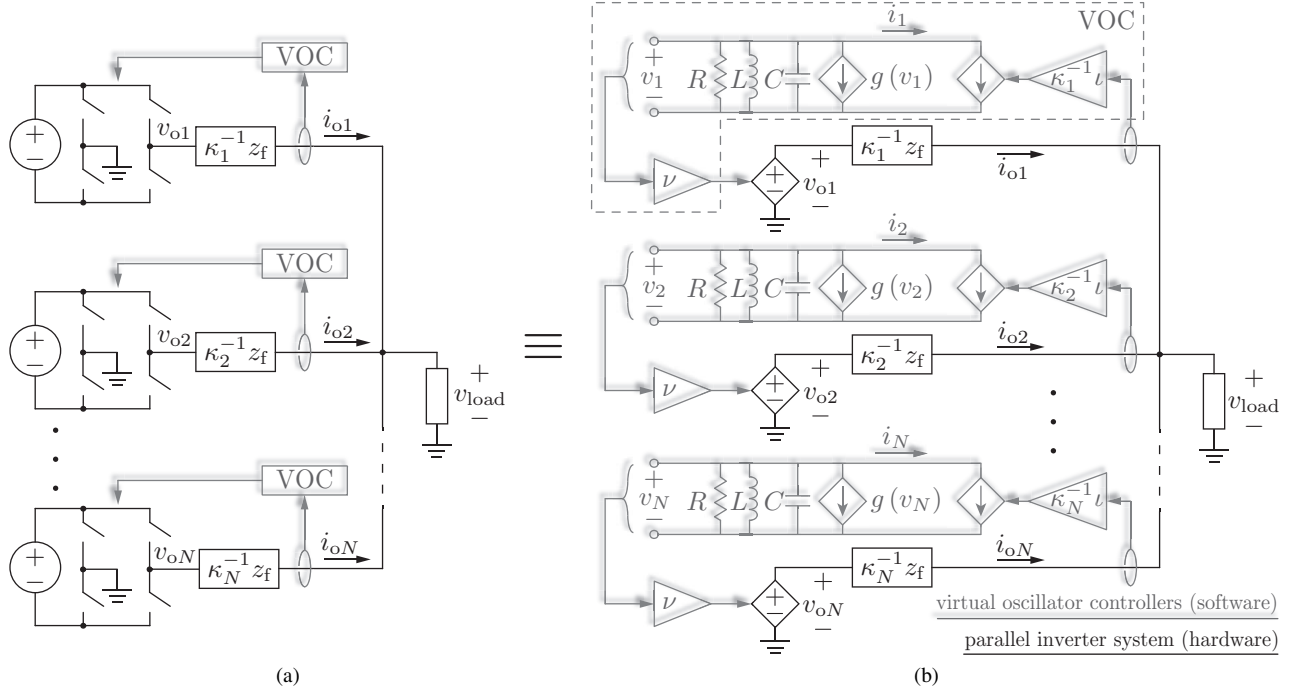


Figure 3: The system of inverters with virtual oscillator control in (a) can be modeled as the system of coupled oscillators shown in (b).

from its respective virtual oscillator. Congruently, the virtual-oscillator terminal voltage is scaled by  $\nu$  to generate the ac voltage command. Note that  $\iota, \nu \in \mathbb{R}$  are referred to as the nominal current and voltage gains, respectively, and they are integral to controller design as explained in Section V; additionally, and as explained next,  $\kappa_j \in \mathbb{R}$ ,  $j = 1, \dots, N$ , are output-filter scaling parameters selected to promote power sharing.

The rated system RMS voltage is denoted by  $V_{\text{rated}}$ , and the power rating of the  $j^{\text{th}}$  inverter is denoted by  $P_j$ . The impedance of the  $j^{\text{th}}$  output filter will be written as  $\kappa_j^{-1} z_f(s)$ , where  $z_f(s)$  is defined as the *reference filter impedance*. The former definitions allow us to establish a *base impedance*,  $z_{\text{base}j} = V_{\text{rated}}^2 / P_j$ , such that the per-unitized  $j^{\text{th}}$  filter impedance is equal to  $z_f(s) / (\kappa_j z_{\text{base}j})$ . By selecting the per-unit filter impedance of each inverter to be identical, it is straightforward to show that

$$\frac{P_j}{\kappa_j} = \frac{P_k}{\kappa_k}, \quad \forall j, k = 1, \dots, N. \quad (13)$$

We will show subsequently in Section IV-B (Remark 2), that this filter-design strategy ultimately facilitates power sharing between the inverters. Additionally, as outlined in [47]–[52], the proposed filter-design strategy also ensures that the relative distortion contributions of the individual inverter output currents are matched, such that the THD of the parallel system is essentially the same as the THD of each individual inverter.

### C. Network Analysis

The vectors of inverter terminal voltages and output currents are denoted by  $v_o = [v_{o1}, \dots, v_{oN}]^T$  and  $i_o = [i_{o1}, \dots, i_{oN}]^T$ ,

respectively. From Fig. 3(a), we see that the output current of the  $j^{\text{th}}$  inverter can be expressed as

$$i_{oj}(s) = \kappa_j z_f^{-1}(s) (v_{oj}(s) - v_{\text{load}}(s)), \quad (14)$$

where  $v_{\text{load}}$  denotes the load voltage. The terminal voltages and output currents of the  $j^{\text{th}}$  inverter are related to those of the  $j^{\text{th}}$  virtual oscillator as follows:

$$\begin{cases} v_{oj}(s) = (\nu) v_j(s), \\ i_{oj}(s) = (\kappa_j / \iota) i_j(s). \end{cases} \quad (15)$$

In subsequent analyses, we will find it useful to note that for the  $j^{\text{th}}$  inverter–virtual-oscillator pair, these scalings imply that impedances have to be scaled by  $(\iota\nu)^{-1} \kappa_j$  when reflected from the physical domain through to the virtual-oscillator domain.

Substituting the inverter currents and voltages from (15) into (14), we see that the oscillator output currents and terminal voltages are related by

$$i_j(s) = z_f^{-1}(s) (\iota\nu v_j(s) - \iota v_{\text{load}}(s)). \quad (16)$$

Solving for  $v_j$ , we obtain

$$v_j(s) = (\iota\nu)^{-1} (z_f(s) i_j(s) + \iota v_{\text{load}}(s)). \quad (17)$$

By defining an *equivalent impedance*,<sup>1</sup>

$$z_{\text{eq}}(s) := \frac{\iota v_{\text{load}}(s)}{N \sum_{\ell=1}^N i_{\ell}(s)}, \quad (18)$$

<sup>1</sup>In general, the definition in (18) captures both linear and nonlinear loads. For instance, notice that for a passive impedance load,  $z_{\text{load}}(s)$ , we have  $z_{\text{eq}}(s) = \iota \times z_{\text{load}}(s)$ .

we can rewrite (17) as follows:

$$v_j(s) = (\iota\nu)^{-1} \left( z_f(s)i_j(s) + z_{\text{eq}}(s) \sum_{\ell=1}^N i_\ell(s) \right). \quad (19)$$

Collecting all oscillator voltages, we obtain

$$v(s) = (\iota\nu)^{-1} (z_f(s)I + z_{\text{eq}}(s)\mathbf{1}\mathbf{1}^T) i(s). \quad (20)$$

Solving for  $i(s)$  in (20), we get

$$i(s) = Y(s)v(s), \quad (21)$$

where the network *admittance matrix*,  $Y(s) \in \mathbb{C}^{N \times N}$ , is given by<sup>2</sup>

$$Y(s) = \alpha(s)I + \beta(s)\Gamma, \quad (22)$$

with  $\alpha(s), \beta(s) \in \mathbb{C}$  defined as

$$\begin{cases} \alpha(s) := \iota\nu (z_f(s) + Nz_{\text{eq}}(s))^{-1}, \\ \beta(s) := \iota\nu z_{\text{eq}}(s) (z_f(s) (z_f(s) + Nz_{\text{eq}}(s)))^{-1}, \end{cases} \quad (23)$$

and  $\Gamma \in \mathbb{R}^{N \times N}$  is the network *Laplacian matrix* given by

$$\Gamma := N\mathbf{1}\mathbf{1}^T = \begin{bmatrix} N-1 & -1 & \dots & -1 \\ -1 & N-1 & \dots & -1 \\ \vdots & \vdots & \ddots & \vdots \\ -1 & -1 & \dots & N-1 \end{bmatrix}. \quad (24)$$

A few properties of the Laplacian matrix that we will find useful include: i)  $\text{rank}(\Gamma) = N - 1$ , ii) the eigenvalues of  $\Gamma$  can be written as  $\lambda_1 < \lambda_2 = \dots = \lambda_N$ , where  $\lambda_1 = 0$  and  $\lambda_j = N$  for  $j = 2, \dots, N$ , and iii)  $\Gamma$  can be diagonalized as  $Q\Lambda Q^T$  where  $Q Q^T = I$ . Additional details are in [43], [53], [54].

We will now seek a system description where the linear and nonlinear portions of the system are clearly compartmentalized. Towards this end, first note that the virtual oscillator voltages can be expressed as

$$\begin{aligned} v(s) &= Z_{\text{osc}}(s) (i_g(s) - i(s)) \\ &= Z_{\text{osc}}(s) (i_g(s) - Y(s)v(s)), \end{aligned} \quad (25)$$

where  $i_g(s) = [i_{g1}(s), \dots, i_{gN}(s)]^T$  with  $i_{gj} = -g(v_j)$  (see Fig. 1),  $Z_{\text{osc}}(s) := z_{\text{osc}}(s)I \in \mathbb{C}^{N \times N}$ , and the second line follows after substituting (21). Solving for  $v(s)$  yields

$$\begin{aligned} v(s) &= (I + Z_{\text{osc}}(s)Y(s))^{-1} Z_{\text{osc}}(s)i_g(s) \\ &=: \mathcal{F}(Z_{\text{osc}}(s), Y(s)) i_g(s), \end{aligned} \quad (26)$$

where  $\mathcal{F} : \mathbb{C}^{N \times N} \times \mathbb{C}^{N \times N} \rightarrow \mathbb{C}^{N \times N}$  is called the *linear fractional transformation*.<sup>3</sup>

Using (26), the network of virtual oscillators can be represented using the block diagram in Fig. 4, where the linear and nonlinear subsystems are compartmentalized in  $\mathcal{F}(Z_{\text{osc}}(s), Y(s))$  and  $g(v) = [g(v_1), \dots, g(v_N)]^T$ , respectively.

<sup>2</sup>An outline of the derivation for  $Y(s)$  is given in Appendix B.

<sup>3</sup>For two systems with transfer matrices denoted by  $A(s)$  and  $B(s)$  (of appropriate dimension), the linear fractional transformation is defined as  $\mathcal{F}(A(s), B(s)) := (I + A(s)B(s))^{-1} A(s)$ . Notice that  $\mathcal{F}(A(s), B(s))$  is the transfer matrix for the equivalent system comprised of the negative feedback interconnection of  $A(s)$  and  $B(s)$ .

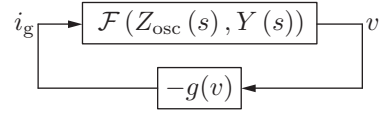


Figure 4: Block-diagram representation of the parallel inverter system with VOC with the linear and nonlinear subsystems clearly compartmentalized.

#### IV. CONDITIONS FOR GLOBAL ASYMPTOTIC SYNCHRONIZATION

In this section, we first derive a coordinate-transformed system based on signal differences. Next, we present the main analytical result of this paper—a condition for synchronization of the inverter terminal voltages in a system controlled with VOC. Finally, we examine the asymptotic dynamics of the synchronized system with a focus on power sharing and circulating currents.

##### A. Corresponding Differential System

*Global asymptotic synchronization* (referred interchangeably as *synchronization* subsequently) in the network of coupled virtual oscillators illustrated in Fig. 3 is defined as the condition

$$\lim_{t \rightarrow \infty} v_j(t) - v_k(t) = 0, \quad \forall j, k = 1, \dots, N. \quad (27)$$

The derivation of sufficient conditions for synchronization can be significantly simplified by examining a corresponding *differential system*, where all signal vectors are multiplied by the projector matrix  $\Pi$  (5). Along these lines, it is clear from (6) that synchronization of the virtual oscillator voltages implies  $\lim_{t \rightarrow \infty} \tilde{v}(t) = \Pi v(t) \rightarrow 0$ .

Beginning with (25), we show in Appendix C that the differential vectors of virtual-oscillator terminal voltages and nonlinear source currents,  $\tilde{v}$  and  $\tilde{i}_g$ , respectively, are related by the same linear fractional transformation in (26), i.e.,

$$\tilde{v}(s) = \mathcal{F}(Z_{\text{osc}}(s), Y(s)) \tilde{i}_g(s). \quad (28)$$

With (28), the differential system can be represented using the block diagram in Fig. 5. Notice that the linear and nonlinear parts of the system are compartmentalized in  $\mathcal{F}(Z_{\text{osc}}(s), Y(s))$  and  $\tilde{g} : \tilde{v} \rightarrow -\tilde{i}_g$ , respectively, where  $\tilde{g}$  captures the effect of the nonlinear voltage-dependent current sources.

##### B. Sufficient Condition for Global Asymptotic Synchronization

We now present a theorem that establishes a sufficient condition for the global asymptotic synchronization of the virtual oscillators as defined in (27). Note that the theorem leverages results presented in [12].

**Theorem 1.** *Consider the network of  $N$  dead-zone oscillators interfaced to the system of parallel inverters with current and voltage gains,  $\iota$  and  $\nu$ , as shown in Fig. 3. The system of oscillators synchronizes in the sense of (27), if*

$$\sup_{\omega \in \mathbb{R}} \left\| \frac{(\iota\nu)^{-1} z_f(j\omega) z_{\text{osc}}(j\omega)}{(\iota\nu)^{-1} z_f(j\omega) + z_{\text{osc}}(j\omega)} \right\|_2 \sigma < 1, \quad (29)$$

where  $z_{\text{osc}}(s)$  is the oscillator linear-subsystem impedance given in (8),  $\sigma$  is the maximum slope of the function  $g(\cdot)$  that describes the nonlinear voltage-dependent current source (11), and  $z_f(s)$  is the reference filter impedance.

*Proof:* Consider the block-diagram of the differential system in Fig. 5. Denoting the differential  $\mathcal{L}_2$  gain of the linear fractional transformation by  $\tilde{\gamma}(\mathcal{F}(Z_{\text{osc}}(s), Y(s)))$ , we have for some non-negative  $\tilde{\eta}$ ,

$$\begin{aligned} \|\tilde{v}\|_{\mathcal{L}_2} &\leq \tilde{\gamma}(\mathcal{F}(Z_{\text{osc}}(s), Y(s))) \|\tilde{i}_g\|_{\mathcal{L}_2} + \tilde{\eta} \\ &\leq \tilde{\gamma}(\mathcal{F}(Z_{\text{osc}}(s), Y(s))) \sigma \|\tilde{v}\|_{\mathcal{L}_2} + \tilde{\eta}, \end{aligned} \quad (30)$$

where the first line in (30) follows from the definition of the differential  $\mathcal{L}_2$  gain in (7), and the second line results from the fact that  $\|\tilde{i}_g\|_{\mathcal{L}_2} \leq \sigma \|\tilde{v}\|_{\mathcal{L}_2}$  for the nonlinear map  $\tilde{g}$  [12]. If we assume that

$$\tilde{\gamma}(\mathcal{F}(Z_{\text{osc}}(s), Y(s))) \sigma < 1, \quad (31)$$

then by isolating  $\|\tilde{v}\|_{\mathcal{L}_2}$  from (30), we obtain

$$\|\tilde{v}\|_{\mathcal{L}_2} \leq \frac{\tilde{\eta}}{1 - \tilde{\gamma}(\mathcal{F}(Z_{\text{osc}}(s), Y(s))) \sigma} < \infty, \quad (32)$$

which implies that  $\tilde{v} \in \mathcal{L}_2$ . Global asymptotic synchronization in the sense of (27) then follows by invoking Barbalat's lemma [42]–[45].

We will now prove that the inequalities in (31) and (29) are equivalent. First, note that by a simple rearrangement of terms, the linear fractional transformation defined in (26) can be expressed equivalently as

$$\mathcal{F}(Z_{\text{osc}}(s), Y(s)) = \mathcal{F}(\zeta(s)I, \beta(s)\Gamma), \quad (33)$$

where we define

$$\zeta(s) := z_{\text{osc}}(s) (1 + \alpha(s)z_{\text{osc}}(s))^{-1}, \quad (34)$$

with  $\alpha(s)$  and  $\beta(s)$  given in (23). From (33), and by definition of the differential  $\mathcal{L}_2$  gain of the linear fractional transformation, we now get

$$\begin{aligned} \tilde{\gamma}(\mathcal{F}(Z_{\text{osc}}(s), Y(s))) &= \tilde{\gamma}(\mathcal{F}(\zeta(s)I, \beta(s)\Gamma)) \\ &= \|\mathcal{F}(\zeta(s)I, \beta(s)\Gamma)\|_{\infty} \\ &= \sup_{\omega \in \mathbb{R}} \frac{\|(I + \zeta(j\omega)\beta(j\omega)\Gamma)^{-1} \zeta(j\omega)\tilde{i}_g(j\omega)\|_2}{\|\tilde{i}_g(j\omega)\|_2} \\ &= \sup_{\omega \in \mathbb{R}} \frac{\|Q(I + \zeta(j\omega)\beta(j\omega)\Lambda)^{-1} \zeta(j\omega)Q^T \tilde{i}_g(j\omega)\|_2}{\|Q^T \tilde{i}_g(j\omega)\|_2}, \end{aligned} \quad (35)$$

where, we have diagonalized  $\Gamma = Q\Lambda Q^T$  and recognized that  $QQ^T = I$  [12]. Notice that the vector  $Q^T \tilde{i}_g(s)$  can be expressed as

$$Q^T \tilde{i}_g(s) = Q^T \Pi i_g(s) = [0, D(s)]^T, \quad (36)$$

where  $D(s) \in \mathbb{C}^{N-1 \times 1}$  is composed of the non-zero elements of  $Q^T \Pi i_g(s)$ . This is because the first column of  $Q$  is given by  $q_1 = \frac{1}{\sqrt{N}} \mathbf{1}$ , and the fact that  $\mathbf{1}^T \Pi = \mathbf{0}^T$ . Defining  $\Lambda_{N-1} = N I_{N-1} \in \mathbb{R}^{(N-1) \times (N-1)}$  ( $I_{N-1}$  is the  $N-1 \times N-1$  identity matrix) to be the diagonal matrix whose entries constitute the

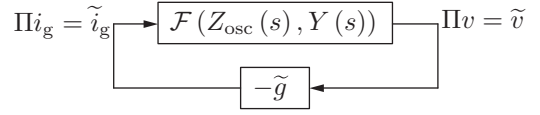


Figure 5: Block-diagram representation of the corresponding differential system.

non-zero eigenvalues of  $\Gamma$ , and substituting (36) in (35), we get

$$\begin{aligned} &\tilde{\gamma}(\mathcal{F}(\zeta(s)I, \beta(s)\Gamma)) \\ &= \sup_{\omega \in \mathbb{R}} \frac{\|(I_{N-1} + \zeta(j\omega)\beta(j\omega)\Lambda_{N-1})^{-1} \zeta(j\omega)D(j\omega)\|_2}{\|D(j\omega)\|_2} \\ &= \sup_{\omega \in \mathbb{R}} (1 + \zeta(j\omega)\beta(j\omega)N)^{-1} \zeta(j\omega) \\ &= \|\mathcal{F}(\zeta(s), \beta(s)N)\|_{\infty}. \end{aligned} \quad (37)$$

Substituting  $\beta(s) = (\alpha(s)z_{\text{eq}}(s))/z_f(s)$  from (23) into  $\mathcal{F}(\zeta(s), \beta(s)N)$ , it is straightforward to show

$$\mathcal{F}(\zeta(s), \beta(s)N) = \frac{(\nu)^{-1} z_f(s) z_{\text{osc}}(s)}{(\nu)^{-1} z_f(s) + z_{\text{osc}}(s)}, \quad (38)$$

which completes the proof. Notice that the synchronization condition in (29) is independent of the number of inverters in the system,  $N$ , as well as the load parameters. It depends only on the impedance of the parallel combination of  $(\nu)^{-1} z_f(s)$  and  $z_{\text{osc}}(s)$ . ■

### C. Asymptotic Dynamics

We now consider the implications of voltage synchronization on power sharing and circulating currents in the system.

*Power Sharing :* Synchronization of the virtual oscillators implies that  $v_j = v_k, \forall j, k = 1, \dots, N$ . Given the relationship between the terminal voltage of the  $j^{\text{th}}$  virtual oscillator and corresponding inverter in (15), we see that synchronization congruently implies  $v_{oj} = v_{ok}, \forall j, k = 1, \dots, N$ , i.e., all the inverter terminal voltages oscillate in phase. Additionally, using (15) and rearranging terms in (14), we obtain

$$v_j(s) = \nu^{-1} (\kappa_j^{-1} z_f(s) i_{oj}(s) + v_{\text{load}}(s)). \quad (39)$$

Synchronization of terminal virtual-oscillator voltages (i.e.,  $v_j = v_k, \forall j, k = 1, \dots, N$ ) further implies

$$(\kappa_j^{-1} z_f(s) i_{oj}(s) + v_{\text{load}}(s)) = (\kappa_k^{-1} z_f(s) i_{ok}(s) + v_{\text{load}}(s)). \quad (40)$$

Simplifying the above expression yields

$$\frac{i_{oj}(s)}{\kappa_j} = \frac{i_{ok}(s)}{\kappa_k}, \quad \forall j, k = 1, \dots, N. \quad (41)$$

Combining (41) with (13), we obtain

$$\frac{i_{oj}(s)}{i_{ok}(s)} = \frac{P_j}{P_k}, \quad \forall j, k = 1, \dots, N. \quad (42)$$

Equation (42) demonstrates that synchronization of virtual oscillator voltages results in current (power) sharing proportional to the power ratings of the inverters. □

*Elimination of Circulating Currents* : We now establish that circulating currents decay to zero as the terminal voltages in the system of parallel inverters synchronize. Adopting the definition of circulating currents proposed in [55], the circulating component of the  $j^{\text{th}}$  inverter output current is denoted by  $i_{cj}(s)$ , and defined as

$$i_{cj}(s) := i_{oj}(s) - \frac{\kappa_j}{\kappa^T \mathbf{1}} i_{\text{load}}(s), \quad (43)$$

where  $\kappa = [\kappa_1, \dots, \kappa_N]^T$ . Since,  $i_{\text{load}}(s) = \sum_{j=1}^N i_{oj}(s) = i_o(s)^T \mathbf{1}$ , (43) can be written as

$$i_{cj}(s) = i_{oj}(s) - \frac{i_o(s)^T \mathbf{1}}{\kappa^T \mathbf{1}} \kappa_j, \quad (44)$$

and the vector of all circulating currents,  $i_c(s) = [i_{c1}(s), \dots, i_{cN}(s)]^T$ , is given by

$$i_c(s) = i_o(s) - \frac{i_o(s)^T \mathbf{1}}{\kappa^T \mathbf{1}} \kappa. \quad (45)$$

Since the terminal voltages of the inverters synchronize asymptotically, in periodic steady state we can write the vector of terminal inverter voltages as  $v_o(s) = \hat{v}_o(s) \mathbf{1}$ , where  $\hat{v}_o(s)$  denotes the synchronized terminal voltage of the inverters. With this notation in place and assuming synchronized operation, we can express the vector of output currents in (14) as

$$\begin{aligned} i_o(s) &= \frac{\hat{v}_o(s) - v_{\text{load}}(s)}{z_f(s)} \text{diag} \{ \kappa_1, \dots, \kappa_N \} \mathbf{1} \\ &= \frac{\hat{v}_o(s) - v_{\text{load}}(s)}{z_f(s)} \kappa. \end{aligned} \quad (46)$$

Substituting (46) in (45), we obtain

$$i_c(s) = \frac{\hat{v}_o(s) - v_{\text{load}}(s)}{z_f(s)} \kappa - \frac{(\hat{v}_o(s) - v_{\text{load}}(s)) \kappa^T \mathbf{1}}{z_f(s) \kappa^T \mathbf{1}} \kappa = \mathbf{0}, \quad (47)$$

which demonstrates that synchronization of the inverter terminal voltages results in the circulating currents decaying to zero in periodic steady state.

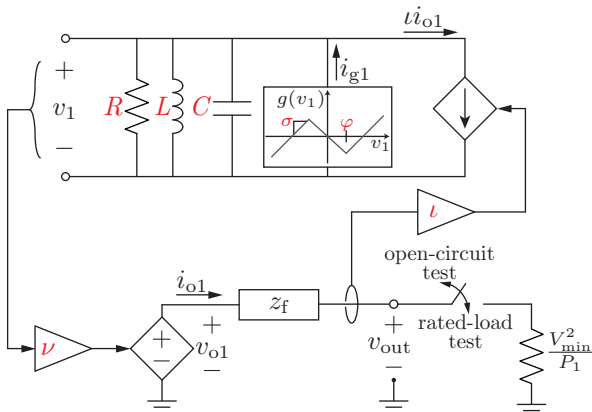


Figure 6: The circuit model used to perform the open-circuit and rated-load tests for parameter selection in inverter 1. The design variables,  $R$ ,  $L$ ,  $C$ ,  $\sigma$ ,  $\varphi$ ,  $\iota$ , and  $\nu$  are highlighted in red.

## V. CONTROLLER PARAMETER SELECTION AND IMPLEMENTATION

In this section, we outline a process for controller parameter selection and subsequent implementation on a microcontroller. Additionally, a technique which facilitates the addition of inverters in an energized system is proposed to improve dynamic performance.

### A. Parameter selection

Without loss of generality and with reference to Fig. 6, we first outline the design strategy for a single inverter in the system (assigned a label index 1). We will fix  $\kappa_1 = 1$ , which implies that the reference impedance for the system,  $z_f(s)$ , is the filter impedance of inverter 1. The design problem can now be formulated as follows: Given the filter impedance,  $z_f(s)$ , power rating,  $P_1$ , and rated system frequency,  $\omega_{\text{rated}}$ , select the current gain,  $\iota$ , voltage gain,  $\nu$ , and virtual oscillator parameters  $R$ ,  $L$ ,  $C$ ,  $\sigma$ , and  $\varphi$ , such that: i) the synchronization condition in (29) is satisfied, and ii) the load voltage is maintained within prescribed upper and lower limits across the complete load range (open circuit to rated load).

Towards this end, we will first pick  $\nu = \sqrt{2}V_{\text{rated}}$ , where  $V_{\text{rated}}$  denotes the rated RMS voltage of the ac system. With this choice, and in light of (15), notice that the virtual oscillator voltages equal the per-unitized output voltages of the corresponding inverters. Oscillations at the rated system frequency,  $\omega_{\text{rated}}$ , result from selecting  $R$ ,  $L$ , and  $C$  such that  $\omega_{\text{rated}}^2 = (LC)^{-1}$  and  $\sigma > 1/R$  (see Section III-A). Next, two simulations are performed with the circuit model in Fig. 6 to ensure the RMS inverter output voltage stays within prescribed upper and lower bounds,  $V_{\text{max}}$  and  $V_{\text{min}}$ , respectively, for the entire load range. The first, is an open-circuit test where the value of  $\varphi$  is tuned until the RMS voltage at the output terminals,  $V_{\text{out}}$ , equals  $V_{\text{max}}$ . Subsequently during the rated-load test, the value of  $\iota$  is adjusted such that  $V_{\text{out}} = V_{\text{min}}$  in steady-state conditions. In general, the designer obtains the desired level of voltage regulation by proper selection of  $\varphi$  and  $\iota$ . In particular, the open-circuit and full-rated-load tests

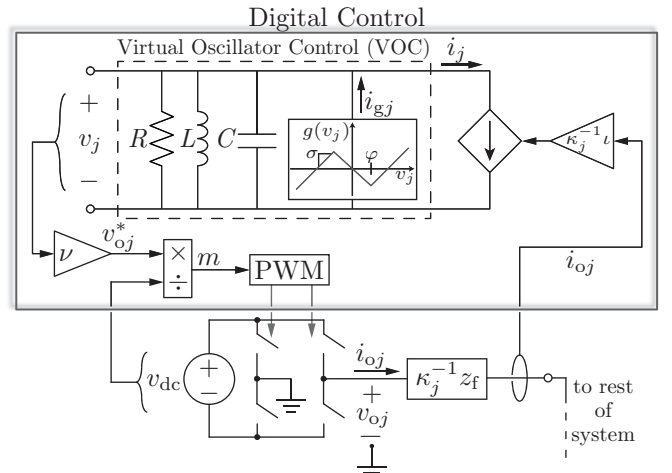


Figure 7: Digital implementation of virtual oscillator control for the  $j^{\text{th}}$  inverter.

ensure that the values of  $\varphi$  and  $\iota$  are chosen in proportion to  $V_{\max}$  and  $(V_{\max} - V_{\min})$ , respectively. Finally, the parameters are tuned to reduce the value of  $\epsilon = \sqrt{L/C}(\sigma - 1/R)$  such that the synchronization condition in (29) is satisfied.

Inverters with differing power ratings are easily accommodated by appropriately selecting the value of  $\kappa_j$  for  $j = 2, \dots, N$  as dictated by (13). Since  $\kappa_1 = 1$ , it follows that  $\kappa_j = P_j/P_1$ . The remaining parameters are identical to those used in inverter 1.

### B. Controller Implementation

After completing the parameter-selection process outlined above, the resulting controller can be implemented straightforwardly on a standard microcontroller, as shown in Fig. 7, by discretizing the second-order system in (12) which describes the dead-zone oscillator dynamics. With reference to the controller depicted in Fig. 7, the measured output current of the  $j^{\text{th}}$  inverter is scaled by  $\kappa_j^{-1}\iota$  and extracted from the virtual oscillator. The resulting oscillator voltage,  $v_j$ , is multiplied by  $\nu$  to generate an ac voltage command, denoted  $v_{oj}^*$ . After normalizing the voltage command with respect to the dc-link voltage, sine-triangle PWM can be applied to the modulation signal,  $m$ , to generate the switching signals. As a result of this strategy, the average inverter ac voltage follows the commanded voltage, i.e.,  $v_{oj} \rightarrow v_{oj}^* = \nu v_j$ . Furthermore, notice from Fig. 7 that the voltage command,  $v_{oj}^*$ , is scaled by the instantaneously measured dc bus voltage,  $v_{dc}$ , thereby ensuring that the dc link dynamics are decoupled from the oscillator-based controller. This strategy follows from well-established methods for decoupling dc-link dynamics from output ac-control dynamics [56]. Notice that the controller only requires the output current and dc-link voltage measurements. Furthermore, the proposed control does not require real and reactive power computations, a phase-locked loop, or any trigonometric functions.

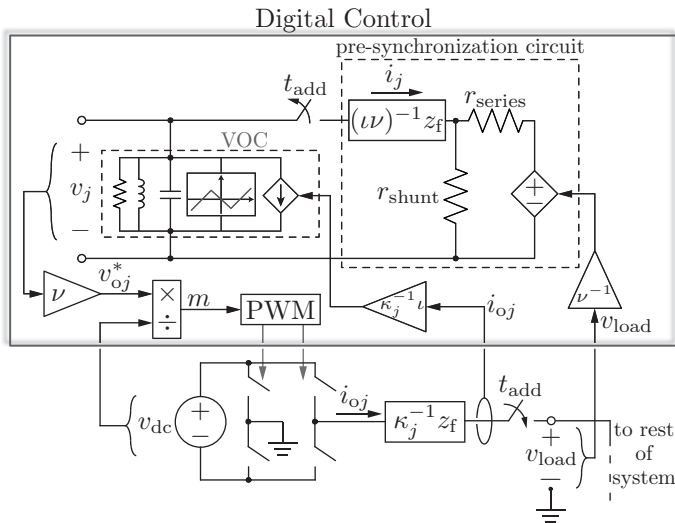


Figure 8: Virtual oscillator controller augmented with a pre-synchronization circuit for the  $j^{\text{th}}$  inverter. The inverter is added to an energized system and the pre-synchronization circuit is removed at  $t = t_{\text{add}}$ .

### C. Facilitating Inverter Addition with a Virtual Pre-Synchronization Circuit

From (29), we see that the condition for global asymptotic synchronization is independent of the number of inverters. This implies that inverters can be added and removed from the system without affecting synchronization in steady state. Although synchronization is guaranteed, system transients can be undesirably large when inverters are added. In this section, we outline a pre-synchronization circuit that can be augmented with the proposed virtual oscillator controller to facilitate the seamless addition of inverters into an energized system with minimal transients.

Assume that for  $t < t_{\text{add}}$ , there are  $N$  synchronized parallel inverters operating in the system. At  $t = t_{\text{add}}$ , we wish to add an additional inverter to the system. As shown in Fig. 8, for  $t < t_{\text{add}}$ , the virtual oscillator controller is connected across a virtual pre-synchronization circuit which consists of: i) a scaled filter impedance,  $(\iota\nu)^{-1}z_f$ , ii) a shunt resistor,  $r_{\text{shunt}}$ , iii) a series resistor,  $r_{\text{series}}$ , and iv) a controlled voltage source which follows the measured value of  $v_{\text{load}}$ .

The purpose of the pre-synchronization circuit is to ensure that the state-variables of the controller associated with the additional inverter are close to synchrony with those of the operational inverters. The design of the pre-synchronization circuit is based on some key observations: i) in steady state, the current through  $r_{\text{series}}$  is approximately zero, and ii) the voltage across  $r_{\text{shunt}}$  closely follows the load voltage. In other words, the pre-synchronization circuit in Fig. 8 ensures that the output current of the virtual oscillator corresponding to the inverter to be added closely follows that of the previously existing virtual oscillators prior to unit addition. To ensure proper operation,  $r_{\text{shunt}}$  must be chosen such that the power it consumes is of the same order of the inverter power rating given by  $(\iota\nu)^{-1}\kappa_j(V_{\text{rated}}^2/P_j)$ , where  $P_j$  is the power rating

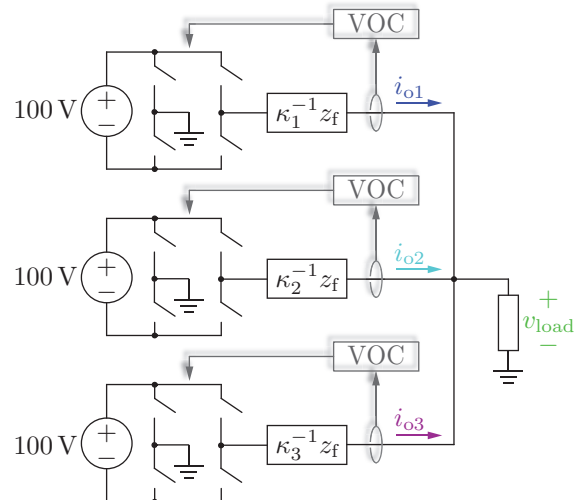


Figure 9: Experimental setup composed of three parallel inverters and load.

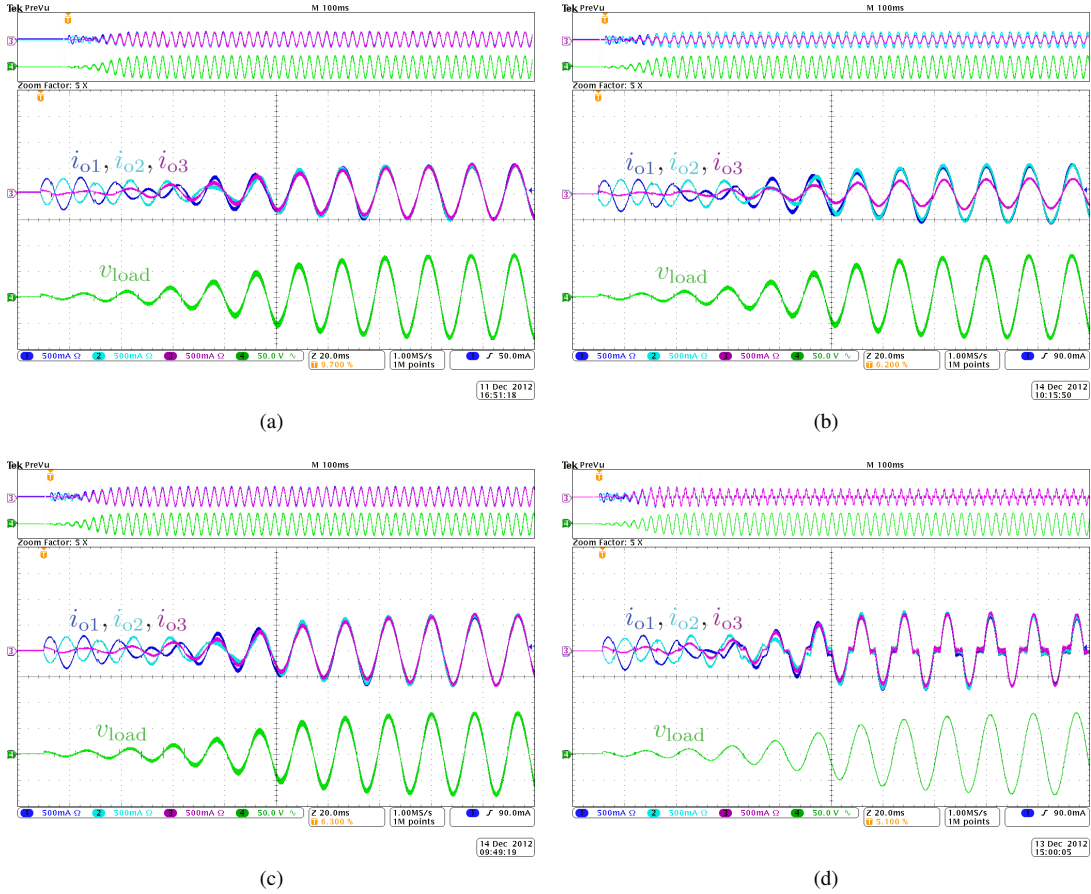


Figure 10: Load voltage and inverter currents during startup with non-identical initial conditions. Waveforms in (a) and (b) demonstrate system behavior when connected to a resistive load under 1 : 1 : 1 and 2 : 2 : 1 ratios of power sharing, respectively. Waveforms in (c) and (d) correspond to the case of equal power sharing with *RLC* and nonlinear diode-bridge rectifier loads, respectively.

of the  $j^{\text{th}}$  inverter.<sup>4</sup> Finally,  $r_{\text{series}}$  should be picked sufficiently small such that a low impedance path exists between the load following voltage source and  $r_{\text{shunt}}$ . When the inverter is added at  $t = t_{\text{add}}$ , the pre-synchronization circuit is disconnected, such that the original VOC controller in Fig. 7 is recovered.

## VI. EXPERIMENTAL RESULTS

The experimental prototype consists of three single-phase inverters connected in parallel. An electrical schematic of the hardware setup is shown in Fig. 9. Each inverter operates at a 25 kHz switching frequency and utilizes an independent virtual oscillator controller implemented on a TMS320F28335 digital signal processor. The differential equations in (12) were discretized using a 100  $\mu\text{s}$  sample step-size. To demonstrate the versatility of the proposed method and validate the analysis presented in Section IV, multiple load types and power sharing ratios are investigated. In particular, we consider resistive, *RLC*, and nonlinear diode-bridge rectifier loads. For the subset of case studies with equal power sharing, it follows that  $\kappa = [1, 1, 1]^T$ . In cases with non-uniform power sharing,

<sup>4</sup>Recall that the factor  $(\iota\nu)^{-1}\kappa_j$  is used to reflect impedances from the physical domain to the virtual-oscillator domain for the  $j^{\text{th}}$  inverter-virtual-oscillator combination.

$\kappa = [1, 1, 1/2]^T$  which implies two of the inverters share 40% of the load, while the third inverter provides 20% of the load power. Subsequently, we refer to the setup with equal sharing as the 1 : 1 : 1 case, and the setup with non-uniform power sharing as the 2 : 2 : 1 case.

The reference filter impedance is given by  $z_f(s) = sL_f + R_f$ , where  $L_f$  is the output-filter inductance and  $R_f$  includes the winding, interconnection, and MOSFET on-state resistances. The virtual-oscillator inductance and capacitance,  $L$  and  $C$ , respectively, were selected for a 60 Hz ac frequency. The upper and lower RMS load voltage limits were selected as  $1.05 \times V_{\text{rated}}$  and  $0.95 \times V_{\text{rated}}$ , respectively, with  $V_{\text{rated}} = 60$  V. Given the allowable load-voltage range and the inverter power ratings given in Table I, the open-circuit and full-rated load tests described in Section V-A were conducted to select  $\varphi$  and  $\iota$ , respectively. The complete list of inverter specifications and design parameters is summarized in Table I. It should be mentioned that the experimental results in this section are a testament to the robustness of the proposed method to electric component tolerances, uncertainty, and round-off error in practical applications.

For the particular filter structure employed, it can be shown that the linear fractional transformation is given by

$$\mathcal{F}(z_{\text{osc}}(s), (\iota\nu)z_f^{-1}(s)) = \frac{a_2s^2 + a_1s}{b_3s^3 + b_2s^2 + b_1s + b_0}, \quad (48)$$

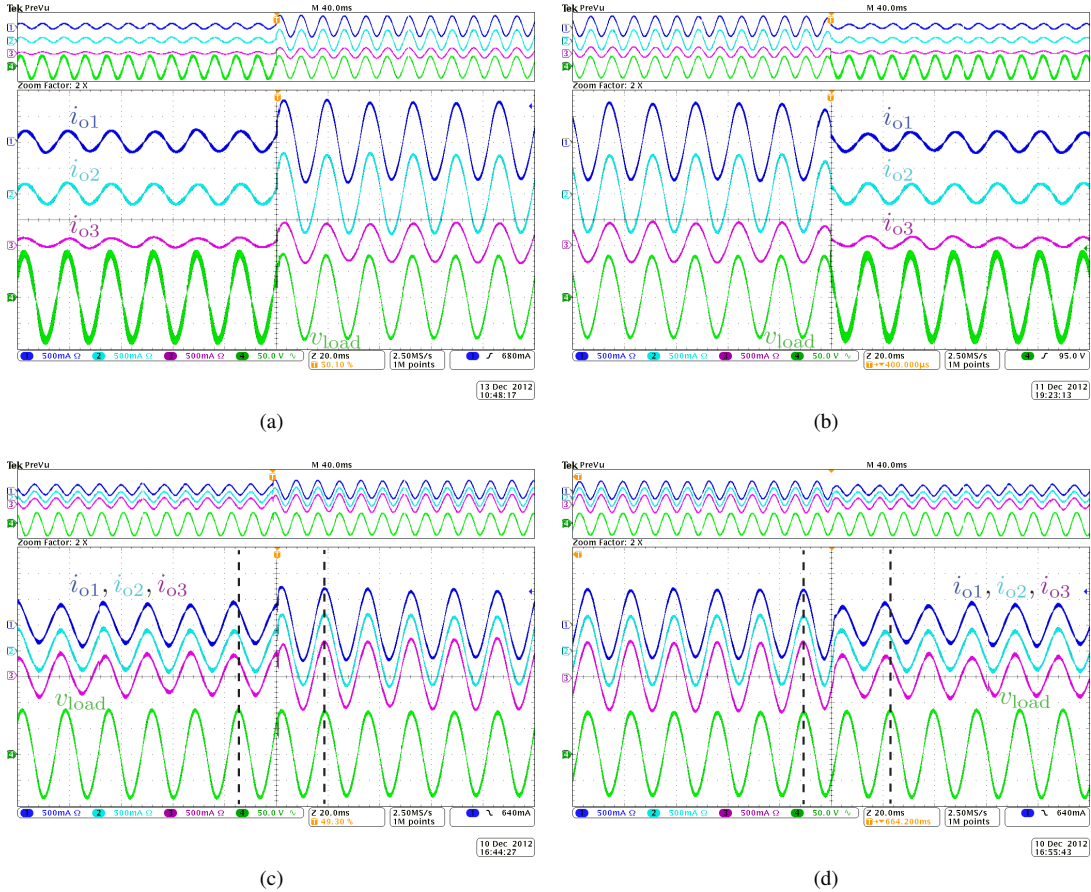


Figure 11: Waveforms in (a) and (b) demonstrate the system transient response with 2 : 2 : 1 power sharing during a step up and step down in resistive load. Waveforms in (c) and (d) correspond to load steps with an  $RLC$  load. The dashed lines illustrate the change in power factor after each load transient. In each case, the load transient occurs at the midpoint of the time axis.

where  $a_2 = L_f$ ,  $a_1 = R_f$ ,  $b_3 = L_f C$ ,  $b_2 = (L_f/R) + R_f C$ ,  $b_1 = (L_f/L) + (R_f/R) + \nu$ , and  $b_0 = R_f/L$ . Evaluating (29) with the values given in Table I, it can be shown that  $\|\mathcal{F}(z_{osc}(j\omega), (\nu)z_f^{-1}(j\omega))\|_{\infty} \sigma = 0.77 < 1$ , which guarantees synchronization.

#### A. Start up

First, we consider the case when all three inverters are simultaneously energized from a cold-start. To emulate errors which may exist in a practical system, each inverter is programmed with non identical initial conditions, i.e., initial conditions for the three virtual oscillator voltages were selected to be  $(1/\nu) [5 \text{ V}, 4 \text{ V}, 3 \text{ V}]^T$ . Figs. 10(a)–10(b) show the inverter currents and load voltage from startup in the presence of a resistive load under uniform and nonuniform sharing, respectively. The waveforms in Figs. 10(c)–10(d) illustrate startup system dynamics with an  $RLC$  load and nonlinear rectifier load, respectively. The  $RLC$  load impedance is given by  $(R_{rlc} + sL_{rlc}) \parallel (R_{rlc} + (sC_{rlc})^{-1})$ ; the values of  $R_{rlc}$ ,  $L_{rlc}$ , and  $C_{rlc}$  are listed in Table I.

#### B. Load transients

System responses to load transients are illustrated in Fig. 11. In particular, Figs. 11(a)–11(b) depict the transient response

to step changes in a resistive load with 2 : 2 : 1 power sharing. It can be observed that the increase in output current is nearly instantaneous with changes in the load and that the load voltage is unperturbed. The waveforms in Figs. 11(c)–11(d) correspond to an  $RLC$  load where the load is changed from  $(R_{rlc} + sL_{rlc}) \parallel (R_{rlc} + (sC_{rlc})^{-1}) \leftrightarrow (R_{rlc} + sL_{rlc})$ . Note that the change in power factor (denoted by dashed lines) coincides with the instant at which the series  $RC$  component of the  $RLC$  load is switched in and out. There are no dc components in the periodic steady-state waveforms.

#### C. Inverter addition and removal

Here we investigate the system dynamics as inverters are removed from and added into an energized system. The virtual pre-synchronization circuit described in Section V-C, and illustrated in Fig. 8 was utilized to facilitate inverter addition. Figs. 12(a) and 12(c) show the transient response as the third inverter is removed from the system with resistive and rectifier loads, respectively. Notice that the remaining inverters abruptly increase their current output when the third inverter is removed, which ensures that the load voltage continues to meet specifications. The waveforms in Figs. 12(b) and 12(d) illustrate system behavior when the third inverter is added into the system. Despite the sudden inclusion of the third inverter,

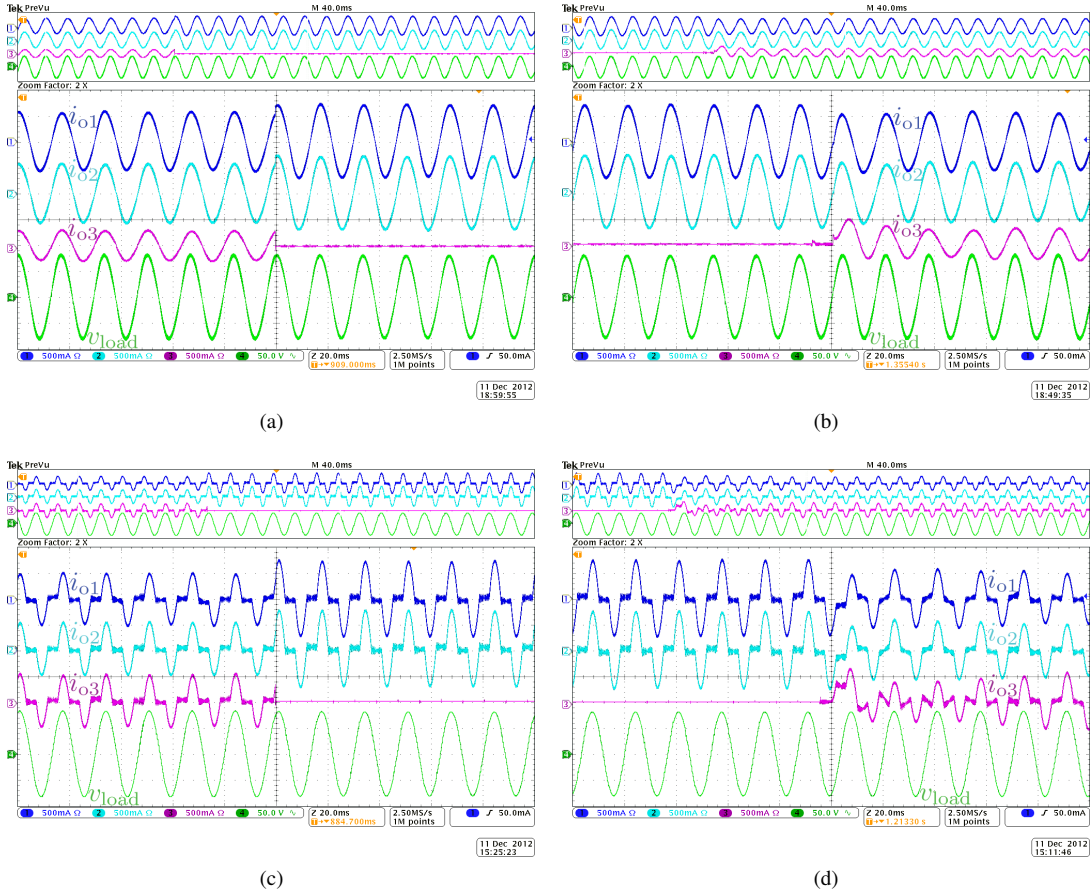


Figure 12: Inverter removal and addition transients. Waveforms (a) and (b) correspond to the system with a resistive load and a sharing ratio of 2 : 2 : 1. Waveforms (c) and (d) show inverter removal and addition dynamics in the presence of a nonlinear rectifier load with 1 : 1 : 1 power sharing. In each case, inverter addition/removal occurs at the midpoint of the time axis.

transients are minimal, and synchronization is achieved in a few cycles.

#### D. Robustness to Parameter Variations

Parametric uncertainty in the proposed approach predominantly arises from two sources: i) small round-off and truncation errors in programming the virtual oscillators within the microcontroller, and ii) filter impedance variations due to manufacturing tolerances and degradation. In [12], it was shown that small errors in the virtual oscillator parameters result in small and bounded voltage synchronization errors. Below, we study the impact of filter impedance deviations on power sharing and circulating currents.

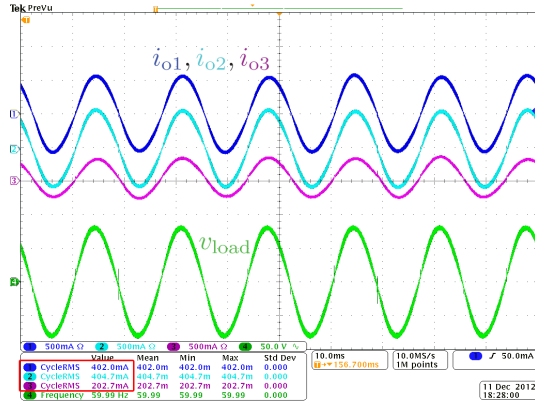
We present a set of comparative experimental results to illustrate the minimal impact of large deviations in output-filter impedances (outside of expected tolerances) on power sharing. As described in Sections III-B and V-A, the per unit impedance of all output filters should ideally be identical. This design choice ultimately results in perfect power sharing between the parallel inverters. The experimental results in Fig. 13 correspond to a system with 2 : 2 : 1 current sharing. In Fig. 13(a), we consider the baseline case where each filter impedance closely matches the nominal required value. In Fig. 13(b), the filter inductance of inverter 3 was intentionally decreased by a factor of 2 from the nominal

value. By comparing the RMS values of the inverter-output currents in the two experiments, it can be confirmed that the power-sharing error introduced by the large filter impedance deviation is negligible. In particular, a 50% change in the filter inductance of inverter 3 only results in a 4% change in the power delivered by that inverter (see the highlighted red boxes in Fig. 13).

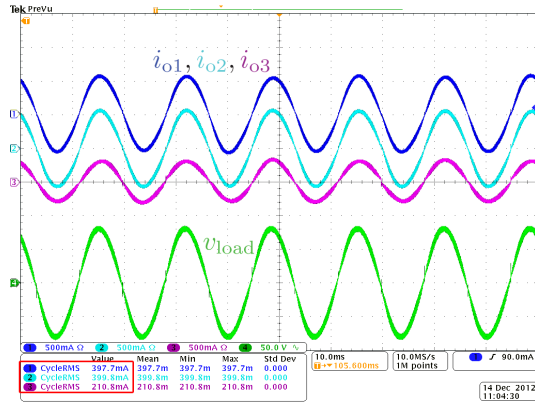
Next, we consider the impact of filter impedance variations on circulating currents. Again, the experimental setup with 2 : 2 : 1 power sharing is analyzed. Adopting the definition in (43), Figs. 14(a) and 14(b) illustrate the circulating components for the nominal filter case and for the case with 50% deviation in the filter inductance of inverter 3. As predicted by the analysis in Section IV-C for the case with perfect voltage synchronization, the waveforms in Fig. 14(a) confirm that the measured circulating components decay to zero. Furthermore, the measurements in Fig. 14(b) show that the circulating currents approach zero despite the large deviation in filter inductance for inverter 3, demonstrating robustness of the proposed approach.

## VII. CONCLUSIONS AND DIRECTIONS FOR FUTURE WORK

A method for controlling a system of parallel single phase inverters without communication was introduced. The pro-



(a)

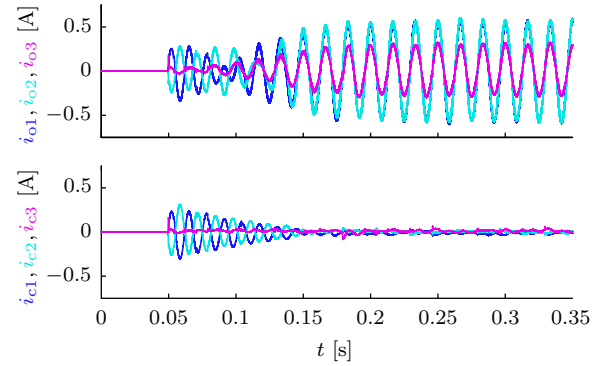


(b)

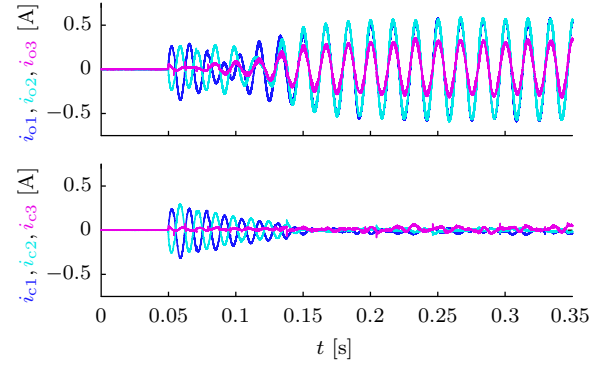
Figure 13: Measurements corresponding to three parallel inverters serving a resistive load with a 2 : 2 : 1 current sharing ratio. The waveforms in (a) correspond to the ideal case where the filter values closely match the nominal values and the results in (b) correspond to the case where the filter inductance of inverter 3 is intentionally reduced by 50% from the nominal value. Despite the large deviation of filter impedance in (b), the impact on current sharing accuracy is negligible. Comparing the two experiments, a modest 4% change in the power delivered by inverter 3 is observed.

posed technique, referred to as virtual oscillator control, relies on programming the controller of each inverter such that the inverter emulates the dynamics of a dead-zone oscillator circuit. It was shown that the system of  $N$  inverters synchronize their ac outputs and share the load in proportion to their power rating without communication. In addition, a method which facilitates the addition of inverters into an energized system was developed. A sufficient condition for virtual oscillator synchronization was derived and the result was shown to be independent of the load and the number of inverters. Experimental results validated the proposed control approach with uniform and non-uniform power sharing between inverters while connected to both linear and nonlinear loads.

Compelling avenues for future work include developing similar virtual-oscillator based controllers for grid connected applications. Furthermore, although there are no practical barriers to the use of  $LC$  and  $LCL$  filters, the analytical framework should be extended to accommodate these additional filter structures. Furthermore, although it was experimentally shown that the proposed method exhibits robustness



(a)



(b)

Figure 14: Measured circulating currents during startup under 2 : 2 : 1 sharing with a resistive load. Nominal filter values were used in (a). In (b), filter inductance 3 was deliberately halved from the nominal design value. In both cases, the circulating currents,  $i_{c1}$ ,  $i_{c2}$ , and  $i_{c3}$ , approach zero with asymptotic voltage synchronization.

to filter parameter deviations, future efforts could be focused on analytically quantifying robustness margins. Finally, while the analysis and experiments in this paper are focused on controller-time-scale synchronization phenomena, it is important to analyze switch-level dynamic phenomena of interest with VOC. It would be of interest to determine whether there are benefits associated with PWM carrier synchronization or dc bus coordination, even though experimental results have shown that these are not required.

## APPENDIX

### A. Experimental parameters

The inverter hardware specifications and control parameters are listed below in Table I. The virtual oscillator parameters are  $R$ ,  $L$ ,  $C$ ,  $\sigma$ , and  $\varphi$ . The voltage and current scaling gains are denoted as  $\nu$  and  $\iota$ , respectively. System voltage and frequency ratings are  $\omega_{\text{rated}}$  and  $V_{\text{rated}}$ , respectively. Using the design procedure in Section V-A, the upper and lower voltage limits are  $V_{\text{max}}$  and  $V_{\text{min}}$ , respectively. The nominal inverter filter impedance is  $z_f(s) = R_f + sL_f$ . The  $j^{\text{th}}$  inverter power rating is denoted as  $P_j$  and the accompanying power rating scaling factors are denoted as  $\kappa_1$ ,  $\kappa_2$ , and  $\kappa_3$ . The maximum rated RMS output current of the nominal inverter design is denoted as  $I_{\text{max}}$ . The pre-synchronization circuit parameters, as described in Section V-C, are denoted as  $r_{\text{series}j}$  and  $r_{\text{shunt}j}$ .

The  $RLC$  load parameters are denoted by  $R_{rlc}$ ,  $L_{rlc}$ , and  $C_{rlc}$ . The resulting voltage regulation curve for the selected parameters is given in Fig. 15.

Table I: Experimental hardware and controller parameters.

$\omega_{\text{rated}} = 2\pi 60 \text{ rad s}^{-1}$	$R_f = 1 \Omega$
$V_{\text{rated}} = 60 \text{ V}$	$L_f = 6 \text{ mH}$
$V_{\text{max}} = 1.05 \times V_{\text{rated}}$	$\kappa_1, \kappa_2 = 1$
$V_{\text{min}} = 0.95 \times V_{\text{rated}}$	$\kappa_3 = 1, \frac{1}{2}$
$R = 10 \Omega$	$I_{\text{max}} = 2^{-\frac{1}{2}} 0.8 \text{ A}$
$L = 500 \mu\text{H}$	$P_j = \kappa_j I_{\text{max}} V_{\text{min}}$
$C = 1 / (L\omega_{\text{rated}}^2)$	$r_{\text{series}j} = 100 \frac{\kappa_j}{\nu} \Omega$
$\sigma = 1 \text{ S}$	$r_{\text{shunt}j} = 2 \frac{P_j}{I_{\text{max}}^2} \frac{\kappa_j}{\nu}$
$\varphi = 0.4695 \text{ V}$	$R_{rlc} = 50 \Omega$
$\iota = 0.1125$	$L_{rlc} = 37 \text{ mH}$
$\nu = \sqrt{2} V_{\text{rated}}$	$C_{rlc} = 48 \mu\text{F}$

### B. Derivation of $Y(s)$

From (20), we see that the inverse of the admittance matrix is given by

$$Y^{-1}(s) = \frac{z_f(s)}{\nu} \left( I + \frac{z_{\text{eq}}(s)}{z_f(s)} \mathbf{1}\mathbf{1}^T \right). \quad (49)$$

For an invertible square matrix  $A$ , and vectors  $x, y$ , the Sherman-Morrison-Woodbury formula [57] states

$$(A + xy^T)^{-1} = A^{-1} - \frac{A^{-1}xy^T A^{-1}}{1 + y^T A^{-1}x}. \quad (50)$$

Applying this to invert (49), we get

$$Y(s) = \frac{\nu}{z_f(s)} \left( I - \frac{(z_{\text{eq}}(s)/z_f(s))\mathbf{1}\mathbf{1}^T}{1 + (z_{\text{eq}}(s)/z_f(s))\mathbf{1}^T\mathbf{1}} \right). \quad (51)$$

Recognizing that  $\mathbf{1}^T\mathbf{1} = N$ , and the fact that  $\mathbf{1}\mathbf{1}^T = N\mathbf{I} - \Gamma$ , we can simplify (51) to obtain

$$Y(s) = \frac{\nu}{z_f(s)(z_f(s) + N z_{\text{eq}}(s))} (z_f(s)I + z_{\text{eq}}(s)\Gamma), \quad (52)$$

which is of the form  $Y(s) = \alpha(s)I + \beta(s)\Gamma$ , with  $\alpha(s)$  and  $\beta(s)$  given in (23).

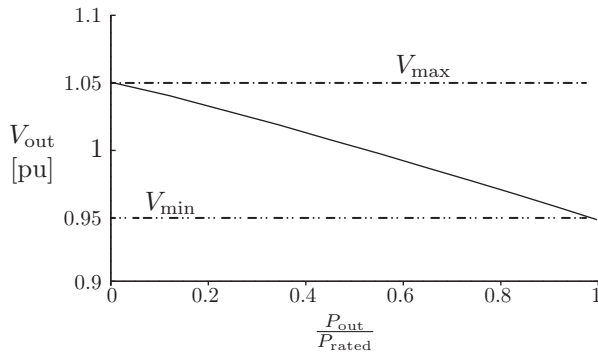


Figure 15: The voltage regulation curve corresponding to the experimental setup. Using the open-circuit and full-rated-load tests, the values of  $\varphi$  and  $\iota$  were tuned such that the load voltage is maintained between  $\pm 5\%$  of the rated value of the entire load range.

### C. Derivation of (28)

Begin by pre-multiplying both sides of (25) by the projector matrix,  $\Pi$ , to obtain

$$\begin{aligned} \Pi v(s) &= \Pi Z_{\text{osc}}(s) (i_g(s) - i(s)) \\ &= Z_{\text{osc}}(s) (\tilde{i}_g(s) - \Pi Y(s)v(s)). \end{aligned} \quad (53)$$

The second line in (53) follows from recognizing that  $\Pi Z_{\text{osc}}(s) = \Pi z_{\text{osc}}(s)I = z_{\text{osc}}(s)\Pi = Z_{\text{osc}}(s)\Pi$ , and substituting for  $i(s)$  from (21). Next, it is straightforward to show that the projector and admittance matrices commute:

$$\begin{aligned} \Pi Y(s) &= \Pi (\alpha(s)I + \beta(s)\Gamma) \\ &= \alpha(s)\Pi + \beta(s)\Pi\Gamma \\ &= \alpha(s)\Pi + \beta(s) \left( I - \frac{1}{N} \mathbf{1}\mathbf{1}^T \right) \Gamma \\ &= \alpha(s)\Pi + \beta(s) \left( \Gamma I - \frac{1}{N} \Gamma \mathbf{1}\mathbf{1}^T \right) \\ &= (\alpha(s)I + \beta(s)\Gamma) \Pi = Y(s)\Pi, \end{aligned} \quad (54)$$

where we have used  $\mathbf{1}\mathbf{1}^T\Gamma = \mathbf{0}\mathbf{0}^T = \Gamma\mathbf{1}\mathbf{1}^T$  (which follows from the fact that the row and column sums of  $\Gamma$  are zero). Using  $\Pi Y(s) = Y(s)\Pi$  in (53), we get

$$\tilde{v}(s) = Z_{\text{osc}}(s) (\tilde{i}_g(s) - Y(s)\tilde{v}(s)). \quad (55)$$

Isolating  $\tilde{v}(s)$ , we can then write

$$\begin{aligned} \tilde{v}(s) &= (I + Z_{\text{osc}}(s)Y(s))^{-1} Z_{\text{osc}}(s)\tilde{i}_g \\ &= \mathcal{F}(Z_{\text{osc}}(s), Y(s))\tilde{i}_g(s). \end{aligned} \quad (56)$$

### REFERENCES

- [1] J.-F. Chen and C.-L. Chu, "Combination voltage-controlled and current-controlled PWM inverters for UPS parallel operation," *IEEE Trans. Power Electron.*, vol. 10, pp. 547–558, Sept. 1995.
- [2] Y. Xue, L. Chang, S. B. Kjaer, J. Bordonau, and T. Shimizu, "Topologies of single-phase inverters for small distributed power generators: An overview," *IEEE Trans. Power Electron.*, vol. 19, pp. 1305–1314, Sept. 2004.
- [3] Y. A. R. I. Mohamed and E. El-Saadany, "Adaptive decentralized droop controller to preserve power sharing stability of paralleled inverters in distributed generation microgrids," *IEEE Trans. Power Electron.*, vol. 23, pp. 2806–2816, Nov. 2008.
- [4] D. De and V. Ramanarayanan, "Decentralized parallel operation of inverters sharing unbalanced and nonlinear loads," *IEEE Trans. Power Electron.*, vol. 25, pp. 3015–3025, Dec. 2010.
- [5] B. Johnson, A. Davoudi, P. Chapman, and P. Sauer, "Microgrid dynamics characterization using the automated state model generation algorithm," in *IEEE Proc. Int. Symp. on Circuits and Syst.*, pp. 2758–2761, June 2010.
- [6] B. Johnson, A. Davoudi, P. Chapman, and P. Sauer, "A unified dynamic characterization framework for microgrid systems," *Electric Power Components and Systems*, vol. 40, pp. 93–111, Nov. 2011.
- [7] R. Bojoi, L. Limongi, D. Ruiu, and A. Tenconi, "Enhanced power quality control strategy for single-phase inverters in distributed generation systems," *IEEE Trans. Power Electron.*, vol. 26, pp. 798–806, Mar. 2011.
- [8] M. Borrega, L. Marroyo, R. Gonzalez, J. Balda, and J. Agorreta, "Modeling and control of a master-slave PV inverter with N-paralleled inverters and three-phase three-limb inductors," *IEEE Trans. Power Electron.*, vol. 28, pp. 2842–2855, June 2013.
- [9] WeiYu, D. Xu, and C. Zhou, "Parallel control of the UPS inverters," in *Applied Power Electron. Conf. and Expo.*, pp. 939–944, 2008.
- [10] A. Bezzolato, M. Carmeli, L. Frosio, G. Marchegiani, and M. Mauri, "Reduction of high frequency zero sequence harmonics in parallel connected PV-inverters," in *European Conf. Power Electron. and Appl.*, pp. 1–10, 2011.

- [11] K.-H. Kim and D.-S. Hyun, "A high performance DSP voltage controller with PWM synchronization for parallel operation of UPS systems," in *Power Electron. Spec. Conf.*, pp. 1–7, 2006.
- [12] B. B. Johnson, S. V. Dhople, A. O. Hamadeh, and P. T. Krein, "Synchronization of nonlinear oscillators in an LTI electrical network," *IEEE Trans. Circuits Syst. I: Fundam. Theory Appl.*, 2013. To Appear.
- [13] B. Johnson, *Control, analysis, and design of distributed inverter systems*. PhD thesis, Univ. of Illinois at Urbana-Champaign, Urbana, IL, May 2013.
- [14] B. B. Johnson, S. V. Dhople, J. L. Cale, A. O. Hamadeh, and P. T. Krein, "Oscillator-based inverter control for islanded three-phase microgrids," *IEEE Journ. Photovoltaics*, 2013. To appear.
- [15] M. Chandorkar, D. Divan, and R. Adapa, "Control of parallel connected inverters in standalone ac supply systems," *IEEE Trans. Ind. Appl.*, vol. 29, pp. 136–143, Jan. 1993.
- [16] R. Lasseter, "Microgrids," in *IEEE Power Eng. Society Winter Meeting*, vol. 1, pp. 305–308, 2002.
- [17] M. Marwali, J.-W. Jung, and A. Keyhani, "Control of distributed generation systems - Part II: Load sharing control," *IEEE Trans. Power Electron.*, vol. 19, pp. 1551–1561, Nov. 2004.
- [18] P. Piagi and R. Lasseter, "Autonomous control of microgrids," in *IEEE Power Eng. Society General Meeting*, vol. 1, pp. 1–8, June 2006.
- [19] K. De Brabandere, B. Bolsens, J. Van den Keybus, A. Woyte, J. Driesen, and R. Belmans, "A voltage and frequency droop control method for parallel inverters," *IEEE Trans. Power Electron.*, vol. 22, pp. 1107–1115, July 2007.
- [20] J. Kim, J. Guerrero, P. Rodriguez, R. Teodorescu, and K. Nam, "Mode adaptive droop control with virtual output impedances for an inverter-based flexible ac microgrid," *IEEE Trans. Power Electron.*, vol. 26, pp. 689–701, Mar. 2011.
- [21] J. Rocabert, A. Luna, F. Blaabjerg, and P. Rodriguez, "Control of power converters in ac microgrids," *IEEE Trans. Power Electron.*, vol. 27, pp. 4734–4749, Nov. 2012.
- [22] C.-T. Lee, C.-C. Chu, and P.-T. Cheng, "A new droop control method for the autonomous operation of distributed energy resource interface converters," *IEEE Trans. Power Electron.*, vol. 28, pp. 1980–1993, Apr. 2013.
- [23] J. Guerrero, L. de Vicuna, J. Matas, M. Castilla, and J. Miret, "A wireless controller to enhance dynamic performance of parallel inverters in distributed generation systems," *IEEE Trans. Power Electron.*, vol. 19, pp. 1205–1213, Sept. 2004.
- [24] J. Lopes, C. Moreira, and A. Madureira, "Defining control strategies for microgrids islanded operation," *IEEE Trans. Power Syst.*, vol. 21, pp. 916–924, May 2006.
- [25] N. Pogaku, M. Prodanovic, and T. C. Green, "Modeling, analysis and testing of autonomous operation of an inverter-based microgrid," *IEEE Trans. Power Electron.*, vol. 22, pp. 613–625, Mar. 2007.
- [26] J. M. Guerrero, J. C. Vasquez, J. Matas, L. G. de Vicuña, and M. Castilla, "Hierarchical control of droop-controlled ac and dc microgrids—A general approach toward standardization," *IEEE Trans. Ind. Electron.*, vol. 58, no. 1, pp. 158–172, 2011.
- [27] J. He and Y. W. Li, "An enhanced microgrid load demand sharing strategy," *IEEE Trans. Power Electron.*, vol. 27, pp. 3984–3995, Sept. 2012.
- [28] Q.-C. Zhong, "Robust droop controller for accurate proportional load sharing among inverters operated in parallel," *IEEE Trans. Ind. Electron.*, vol. 60, pp. 1281–1290, April 2013.
- [29] Y. Kuramoto, *Chemical Oscillations, Waves, and Turbulence*. New York: Springer-Verlag, 1984.
- [30] D. C. Michaels, E. P. Matyas, and J. Jalife, "Mechanisms of sinoatrial pacemaker synchronization—a new hypothesis," *Circulation Res.*, vol. 61, pp. 704–714, Nov. 1987.
- [31] K. Wiesenfeld, P. Colet, and S. H. Strogatz, "Frequency locking in Josephson arrays: Connection with the Kuramoto model," *Phys. Rev. E*, vol. 57, pp. 1563–1569, Feb. 1998.
- [32] S. H. Strogatz, *Nonlinear Dynamics And Chaos: With Applications To Physics, Biology, Chemistry, And Engineering*. Studies in nonlinearity, Westview Press, First ed., Jan. 2001.
- [33] F. Dörfler and F. Bullo, "Exploring synchronization in complex oscillator networks," in *IEEE Conf. on Decision and Control*, (Maui, HI, USA), pp. 7157–7170, Dec. 2012.
- [34] F. Dörfler and F. Bullo, "Synchronization and transient stability in power networks and non-uniform Kuramoto oscillators," *SIAM Journ. on Control and Optimization*, vol. 50, pp. 1616–1642, June 2012.
- [35] J. W. Simpson-Porco, F. Dörfler, and F. Bullo, "Synchronization and power sharing for droop-controlled inverters in islanded microgrids," *Automatica*, 2013. In Press.
- [36] N. Ainsworth and S. Grijalva, "A structure-preserving model and sufficient condition for frequency synchronization of lossless droop inverter-based AC networks," *IEEE Trans. Power Syst.*, 2013. in press.
- [37] L. A. B. Tôrres, J. P. Hespanha, and J. Moehlis, "Power supplies synchronization without communication," in *Proc. of the Power and Energy Society General Meeting*, July 2012.
- [38] A. Pogromsky and H. Nijmeijer, "Cooperative oscillatory behavior of mutually coupled dynamical systems," *IEEE Trans. Circuits Syst. I: Fundam. Theory Appl.*, vol. 48, pp. 152–162, Feb. 2001.
- [39] G.-B. Stan, *Global analysis and synthesis of oscillations: A dissipativity approach*. PhD thesis, Univ. of Liege, Belgium, May 2005.
- [40] G.-B. Stan and R. Sepulchre, "Analysis of interconnected oscillators by dissipativity theory," *IEEE Trans. Autom. Control*, vol. 52, pp. 256–270, Feb. 2007.
- [41] M. Arcak, "Passivity as a design tool for group coordination," *IEEE Trans. Autom. Control*, vol. 52, pp. 1380–1390, Aug. 2007.
- [42] A. Dhawan, A. Hamadeh, and B. Ingalls, "Designing synchronization protocols in networks of coupled nodes under uncertainty," in *American Control Conf.*, pp. 4945–4950, June 2012.
- [43] A. Hamadeh, *Constructive Robust Synchronization of Networked Control Systems*. PhD thesis, Cambridge University, UK, June 2010.
- [44] A. Hamadeh, G.-B. Stan, and J. Gonçalves, "Constructive Synchronization of Networked Feedback Systems," in *IEEE Conf. on Decision and Control*, pp. 6710–6715, Dec. 2010.
- [45] H. Khalil, *Nonlinear Systems*. Upper Saddle River, NJ: Prentice Hall, Third ed., 2002.
- [46] A. Van der Schaft, *L2-Gain and Passivity Techniques in Nonlinear Control*. Lecture Notes in Control and Information Sciences, London, UK: Springer, 1996.
- [47] M. Liserre, F. Blaabjerg, and A. Dell'Aquila, "Step-by-step design procedure for a grid-connected three-phase PWM voltage source converter," *International Journ. of Electron.*, vol. 91, no. 8, pp. 445–460, 2004.
- [48] M. Liserre, F. Blaabjerg, and S. Hansen, "Design and control of an LCL-filter-based three-phase active rectifier," *IEEE Trans. Ind. Appl.*, vol. 41, pp. 1281–1291, Sept. 2005.
- [49] B. Parikshith and V. John, "Higher order output filter design for grid connected power converters," in *National Power Systems Conf.*, vol. 1, pp. 614–619, Dec. 2008.
- [50] P. Channegowda and V. John, "Filter optimization for grid interactive voltage source inverters," *IEEE Trans. Ind. Electron.*, vol. 57, pp. 4106–4114, Dec. 2010.
- [51] R. Teodorescu, M. Liserre, and P. Rodríguez, *Grid Converters for Photovoltaic and Wind Power Systems*. West Sussex, UK: Wiley, 2011.
- [52] Y. Tang, P. C. Loh, P. Wang, F. H. Choo, F. Gao, and F. Blaabjerg, "Generalized design of high performance shunt active power filter with output LCL filter," *IEEE Trans. Ind. Electron.*, vol. 59, pp. 1443–1452, Mar. 2012.
- [53] L. B. Cremean and R. M. Murray, "Stability analysis of interconnected nonlinear systems under matrix feedback," in *Proc. IEEE Conf. on Decision and Control*, vol. 3, pp. 3078–3083, Dec. 2003.
- [54] R. Olfati-Saber and R. M. Murray, "Consensus problems in networks of agents with switching topology and time-delays," *IEEE Trans. Autom. Control*, vol. 49, pp. 1520–1533, Sept. 2004.
- [55] C.-T. Pan and Y.-H. Liao, "Modeling and control of circulating currents for parallel three-phase boost rectifiers with different load sharing," *IEEE Trans. Ind. Electron.*, vol. 55, no. 7, pp. 2776–2785, 2008.
- [56] A. Yazdani and R. Iravani, *Voltage-Sourced Converters in Power Systems*. Wiley, 2010.
- [57] R. A. Horn and C. R. Johnson, *Matrix Analysis*. Cambridge University Press, 2013.